

Robust Grid-Forming Control Based on Virtual Flux Observer

Xueqing Gao

Global College

Shanghai Jiao Tong University

Shanghai, China

gaoxq113@sjtu.edu.cn

Jun Zhang

Global College

Shanghai Jiao Tong University

Shanghai, China

zhangjun12@sjtu.edu.cn

Tao Li

Spintrol

Shanghai, China

tao.li@spintrol.com

Mingming Zhang

Student Innovation Center

Shanghai Jiao Tong University

Shanghai, China

brucechang@sjtu.edu.cn

Abstract—This paper investigates the design and analysis of a novel grid-forming (GFM) control method for grid-connected converters (GCCs). The core novelty lies in a virtual flux observer-based synchronization and load angle control method. The terminal voltage of the converter is directly regulated to provide voltage-source behavior. The control parameters are designed for decoupling and pole placement. The proposed method exhibits strong robustness in stability and dynamical performance across varying and uncertain grid strengths. The robust control performance of the proposed method is first demonstrated by small-signal analysis, then validated by experiments on a 20 kVA power conversion system.

Index Terms—grid-forming control, grid synchronization, virtual flux observer, stability, robustness, sensorless

I. INTRODUCTION

In modern power systems with a growing share of distributed generation (DG), grid connected converters (GCCs) controlled by traditional grid-following (GFL) strategies face increasing stability risks, particularly under weak grid conditions or parallel operation [1]. The grid-forming (GFM) controllers have therefore been suggested as an effective solution for stable integration of DG units at weak points of common coupling (PCC) [2], [3].

Two defining characteristics of GFM converters are their voltage-source behavior and strong coupling between active power and grid synchronization. The former is realized by direct manipulation of converter terminal voltage, while the latter is rooted in power-synchronization control (PSC), which emulates the droop mechanism of synchronous generators [4], [5]. Although voltage-source behavior and PSC enables stable operation under weak grid condition, recent studies have revealed that GFM controllers also lack stability robustness [6], [7]. The most notable issue is the degradation of control performance under strong grid condition, including limited bandwidth and low frequency oscillation, which are resulted by increased sensitivity of active power to load angle perturbations [8], [9].

Various remedies have been proposed to enhance stability robustness of GFM controllers with respect to grid strength. For example, current reference feedforward [10] or implicit current loop [11] are incorporated into PCC voltage controller to improve dynamic performance under strong grid condition; in [12], PSC is hybridized with phase-locked loop (PLL),

which can be used for synchronization under strong grid condition to ensure stable operation. However, these approaches merely refine existing control loops without changing the nature of power synchronization, and may further complicate parameter tuning and dynamic performance of closed-loop system [8], [13].

Recently, some disturbance observer-based GFM controllers have been proposed, which obtained satisfying performances in sensorless and multifunctional GCC control [14]–[16]. However, these methods still adopt the traditional PSC for synchronization, or adopt arbitrarily defined reference frames. Therefore, the stability robustness limitation of existing GFM controller is not thoroughly addressed.

Potentially, grid synchronization can be incorporated in observers based on mathematical model of the GCC. In contrast to non-model-based synchronization mechanisms of GFL and GFM, observer-based synchronization makes full use of available model information, such as filter topology and nominal impedance. Therefore, stability margin and dynamic performance can be actively shaped, which potentially overcomes the stability robustness limitations of existing GCC control paradigms.

Conceptually, the task of grid synchronization is much similar to position estimation in electrical drives. Moreover, the mathematical models of permanent-magnet synchronous machines (PMSMs) and grid-connected converters (GCCs) share strong structural similarity, which facilitates the transfer of mature PMSM sensorless control techniques [17], [18], such as flux observer, into GCC applications. Therefore, this article makes an attempt at improving the stability robustness of GFM controllers with virtual flux observer-based synchronization.

II. MATHEMATICAL MODELING OF THE GCC

Fig. 1 shows the circuit topology and block diagram of the proposed GFM converter, where L is the total impedance including filter impedance and grid impedance.

A. Current model of the GCC

The mathematical model of the GCC in two-phase stationary frame ($\alpha\beta$ -frame) is

$$\begin{aligned} \dot{\mathbf{i}}^s &= (\mathbf{u}_c^s - \mathbf{u}_g^s)/L, \quad \mathbf{u}_g^s = e^{\theta_g \mathbf{J}} \mathbf{u}_g^g, \\ \dot{\theta}_g &= \omega_g, \quad \mathbf{u}_g^g = [U_g \quad 0]^T, \end{aligned} \quad (1)$$

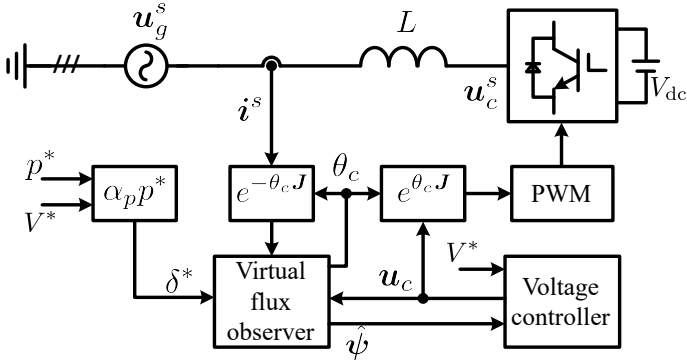


Fig. 1. Circuit topology of GCC and block diagram of the proposed GFM controller. Superscript s denotes variables in $\alpha\beta$ -frame.

where i^s is converter output current, u_c^s is converter output voltage, u_g^s is grid voltage with frequency ω_g , phase angle θ_g and amplitude U_g .

The variables are then transformed into the controller coordinate frame (dq -frame), which rotates at frequency ω_c and phase angle θ_c as shown in Fig. 2,

$$i = e^{-\theta_c J} i^s, \quad u_c = e^{-\theta_c J} u_c^s, \quad u_g = e^{-\theta_c J} u_g^s. \quad (2)$$

Define the angle difference between the grid and controller reference frames as $\delta = \theta_c - \theta_g$, and substitute Eq. (2) into Eq. (1), the mathematical model of GCC in dq -frame is

$$\begin{aligned} \dot{i} &= -\omega_c J i + (u_c - u_g)/L, \\ \dot{\delta} &= \omega_c - \omega_g, \quad u_g = e^{-\delta J} u_g^s, \end{aligned} \quad (3)$$

where δ is included as a state variable.

Active power and PCC voltage magnitude are defined as

$$p = \kappa u_g^T i, \quad \kappa = 3/2, \quad (4a)$$

$$V = (u_c^T u_c)^{1/2}. \quad (4b)$$

B. Virtual flux model of the GCC

The virtual flux of GCC is defined as

$$\psi = L i + \psi_g, \quad \psi_g = (\omega_g J)^{-1} u_g. \quad (5)$$

Substitute Eq. (5) into Eq. (3), the dynamics of virtual flux is

$$\dot{\psi} = -\omega_c J \psi + u_c. \quad (6)$$

III. SYNCHRONIZATION THROUGH VIRTUAL FLUX OBSERVER

From Section II. B, the position of grid voltage vector is contained in virtual flux vector. Therefore, in this section, a synchronous rotating frame is obtained from virtual flux observer for the purpose of active power control.

A. Operating points in controller coordinate frame

First, the desired operating points of u_c , u_g and controller frame position δ in Fig. 2 corresponding to active power set-point p^* and voltage amplitude set-point V^* are specified.

For simplicity, the steady-state of converter voltage aligns with d -axis in steady-state, *i.e.*, $u_c^* = [V^*; 0]$. To maintain

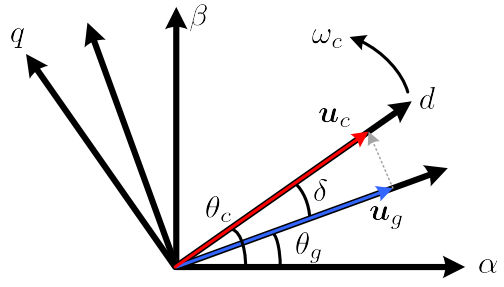


Fig. 2. Definition of controller coordinate frame and load angle δ .

synchronization with the grid voltage, it is required that $\omega_c^* = \omega_g$. Then, let the right hand side of Eq. (6) equals 0 , the desired steady-state of virtual flux is $\psi^* = (\omega_g J)^{-1} u_c^*$.

Let the load angle corresponding to p^* be δ^* , then $u_g^* = e^{-\delta^* J} u_g^s$. Substitute Eq. (5) into Eq. (4a) with steady-state values,

$$p^* = \kappa u_g^{*T} \psi^* / L = \frac{\kappa U_g V^*}{\omega_g L} \sin \delta^*. \quad (7)$$

Therefore, δ^* is almost linearly related to p^* ,

$$\delta^* = \sin^{-1}(\alpha_p p^*) \approx \alpha_p p^*, \quad \alpha_p = \frac{\omega_g L}{\kappa U_g V^*}. \quad (8)$$

B. Virtual flux observer

The virtual flux observer is constructed from Eq. (6) as

$$\dot{\psi} = -\omega_c J \psi + u_c + \mathbf{K}_o e, \quad (9a)$$

$$e = L i + \psi_g^* - \hat{\psi}, \quad \psi_g^* = (\omega_0 J)^{-1} u_g^*, \quad (9b)$$

where ω_0 is the nominal grid frequency.

The grid frequency estimation ω_c is given by a proportional-integral (PI) regulator driven by e ,

$$\dot{\gamma} = e, \quad \omega_c = \mathbf{k}_i \gamma + \mathbf{k}_p e. \quad (10)$$

The phase angle of controller coordinate frame is $\dot{\theta}_c = \omega_c$.

C. Error dynamics and gain design

The estimation errors are defined as

$$\tilde{\psi} = \psi - \hat{\psi}, \quad \tilde{\theta} = \delta - \delta^*, \quad \tilde{\omega} = \omega_c - \omega_g. \quad (11)$$

Their dynamic equations can be derived as

$$\dot{\tilde{\psi}} = -(\omega_g + \tilde{\omega}) J \tilde{\psi} - \mathbf{K}_o e, \quad (12a)$$

$$\dot{\tilde{\theta}} = \tilde{\omega}, \quad (12b)$$

$$\dot{\tilde{\omega}} = \mathbf{k}_i e + \mathbf{k}_p \dot{e}, \quad (12c)$$

where Eq. (12c) holds with the assumption $\dot{\omega}_g = 0$.

Eq. (12) is a nonlinear system with state variables $x = [\tilde{\psi}; \tilde{\theta}; \tilde{\omega}]$. It can be linearized around desired equilibrium $x_0^* = [0; 0; 0]$. First, consider e as an input, and obtain

$$\dot{\tilde{\psi}} = -\omega_0 J \Delta \tilde{\psi} - \mathbf{K}_o \Delta e, \quad (13a)$$

$$\dot{\tilde{\theta}} = \Delta \tilde{\omega}, \quad (13b)$$

$$\dot{\tilde{\omega}} = \mathbf{k}_i \Delta e + \mathbf{k}_p \Delta \dot{e}. \quad (13c)$$

where Δ denotes perturbations. Then, Eq. (9b) is linearized around \mathbf{x}_0^* as

$$\Delta e = \Delta \tilde{\psi} + \mathbf{J} \psi_g^* \Delta \tilde{\theta}. \quad (14)$$

Substitute Eq. (14) into Eq. (13a), the dynamic equation of virtual flux estimation error becomes

$$\Delta \dot{\tilde{\psi}} = -(\omega_0 \mathbf{J} + \mathbf{K}_o) \Delta \tilde{\psi} - \mathbf{K}_o \mathbf{J} \psi_g^* \Delta \tilde{\theta}, \quad (15)$$

where the second term can be canceled by choosing $\mathbf{K}_o = \mathbf{k}_o \psi_g^{*T}$. This gain design decouples the dynamics of synchronization from that of virtual flux estimation, resulting in

$$\Delta \dot{\tilde{\psi}} = -(\omega_0 \mathbf{J} + \mathbf{K}_o) \Delta \tilde{\psi}. \quad (16)$$

The gain vector \mathbf{k}_o can be calculated by solving a pole placement problem defined as

$$\text{eig}(-\omega_0 \mathbf{J} - \mathbf{k}_o \psi_g^{*T}) = \sigma_o, \quad (17)$$

where σ_o specifies two poles on left half of s -plane.

Decoupling properties can also be achieved for grid frequency estimation. Substitute Eq. (14) into Eq. (13c),

$$\Delta \dot{\tilde{\omega}} = (\mathbf{k}_i \Delta \tilde{\psi} + \mathbf{k}_p \Delta \dot{\tilde{\psi}}) + \mathbf{k}_i \mathbf{J} \psi_g^* \Delta \tilde{\theta} + \mathbf{k}_p \mathbf{J} \psi_g^* \Delta \tilde{\omega}. \quad (18)$$

Substitute Eq. (16) in Eq. (18), the first term of Eq. (18) can be canceled if \mathbf{k}_p and \mathbf{k}_i satisfies

$$(\mathbf{k}_i - \mathbf{k}_p (\omega_0 \mathbf{J} + \mathbf{K}_o)) \Delta \tilde{\psi} \equiv \mathbf{0}. \quad (19)$$

Therefore, gains of the PI regulator satisfying

$$\mathbf{k}_i = \mathbf{k}_p (\omega_0 \mathbf{J} + \mathbf{K}_o) \quad (20)$$

decouples the error convergence dynamics of virtual flux estimation from that of frequency estimation.

D. Synchronization properties

The small-signal model of synchronization after decoupling is shown in Fig. 3, where $\Delta \omega_g$ is considered as a disturbance input around nominal frequency ω_0 , *i.e.*, $\omega_g = \omega_0 + \Delta \omega_g$. Using $\Delta \tilde{\theta} = \Delta \delta - \Delta \delta^*$ and $\Delta \tilde{\omega} = \Delta \omega_c - \Delta \omega_g$, the dynamics of synchronization is described by the transfer function matrix

$$\begin{bmatrix} \Delta \delta(s) \\ \Delta \omega_c(s) \end{bmatrix} = \frac{1}{D_1(s)} \begin{bmatrix} -a_2 & -s \\ -a_2 s & -a_1 s - a_2 \end{bmatrix} \begin{bmatrix} \Delta \delta^*(s) \\ \Delta \omega_g(s) \end{bmatrix}, \quad (21)$$

$$a_1 = \mathbf{k}_p \mathbf{J} \psi_g^*, \quad a_2 = -\omega_0 \mathbf{k}_p \psi_g^*.$$

The characteristic polynomial is $D_1(s) = s^2 - a_1 s - a_2$. By final value theorem, the static gain of Eq. (21) is

$$\begin{bmatrix} \Delta \delta(\infty) \\ \Delta \omega_c(\infty) \end{bmatrix} = \begin{bmatrix} 1 & 0 \\ 0 & 1 \end{bmatrix} \begin{bmatrix} \Delta \delta^* \\ \Delta \omega_g \end{bmatrix}, \quad (22)$$

which ensures that the controller coordinate frame converges to the grid reference frame with the same rotational speed ω_g and desired load angle δ^* .

The dynamic performance of synchronization is adjustable by tuning the gain vector \mathbf{k}_p . One simple way is to specify desired bandwidth ω_s and damping ratio ζ of the second-order characteristic polynomial. Let

$$D_1(s) = s^2 - a_1 s - a_2 = s^2 + 2\zeta\omega_s s + \omega_s^2, \quad (23)$$

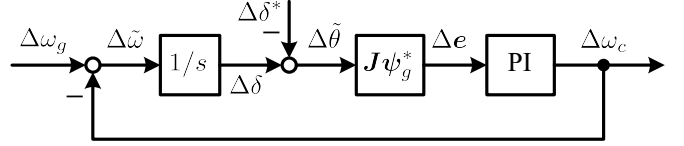


Fig. 3. Small-signal model of grid synchronization after decoupling.

the corresponding gain \mathbf{k}_p can be calculated as

$$\mathbf{k}_p = \left(\begin{bmatrix} \psi_g^{*q} & -\psi_g^{*d} \\ \psi_g^{*d} & \psi_g^{*q} \end{bmatrix}^{-1} \begin{bmatrix} 2\zeta\omega_s \\ \omega_s^2/\omega_0 \end{bmatrix} \right)^T. \quad (24)$$

IV. VOLTAGE CONTROL AND CLOSED-LOOP SYSTEM ANALYSIS

A. Voltage control law and gain design

The converter output voltage is designed as

$$\mathbf{u}_c = \mathbf{u}_c^* + \mathbf{k}_v (V^* - \hat{V}), \quad \hat{V} = \omega_c \left(\hat{\psi}^T \hat{\psi} \right)^{1/2}. \quad (25)$$

To study parameter design, Eq. (25) is first linearized as

$$\Delta \mathbf{u}_c \approx -\mathbf{k}_v \left(\psi_0 \Delta \omega_c + \frac{\omega_0}{\psi_0} \psi_0^T \Delta \psi \right), \quad (26)$$

where $\psi_0 = V^*/\omega_0$, $\psi_0 = \psi^*$. The approximation is resulted from $\Delta \hat{\psi} \approx \Delta \psi$, which is reasonable with high bandwidth of virtual flux estimation. PCC voltage magnitude Eq. (4b) is linearized as

$$\Delta V = \frac{1}{V^*} \mathbf{u}_c^{*T} \Delta \mathbf{u}_c. \quad (27)$$

Substitute Eq. (26) into Eq. (27), it is obvious that the closed-loop poles of ΔV can be equivalently assigned through pole placement for $\Delta \psi$. To this end, Eq. (5) is linearized as

$$\Delta \dot{\psi} = -\omega_0 \mathbf{J} \Delta \psi + \Delta \mathbf{u}_c - \mathbf{J} \psi_0 \Delta \omega_c. \quad (28)$$

Substitute Eq. (26) into Eq. (28),

$$\Delta \dot{\psi} = -(\omega_0 \mathbf{J} + \mathbf{k}_v \mathbf{w}) \Delta \psi - (\mathbf{J} \psi_0 + \psi_0 \mathbf{k}_v) \Delta \omega_c, \quad (29)$$

where $\mathbf{w} = [0 \ -\omega_0]$. Therefore, \mathbf{k}_v can be designed through pole placement such that

$$\text{eig}(-\omega_0 \mathbf{J} - \mathbf{k}_v \mathbf{w}) = \sigma_v, \quad (30)$$

where σ_v specifies two poles on left half of s -plane.

B. Derivation of closed-loop system

The small-signal model of the closed-loop system is shown in Fig. 4. The small-signal state-space models of the component systems can be derived conveniently from Eq. (9), Eq. (25) and Eq. (3). Then, the subsystems are connected according to the input-output relations specified in Fig. 4 to obtain the closed-loop model.

Due to space limitations, the mathematical details are not presented in this article. For stability analysis, the eigenvalues of the closed-loop system matrix are used as indicators. Numerical results of closed-loop stability will be presented in the following section.

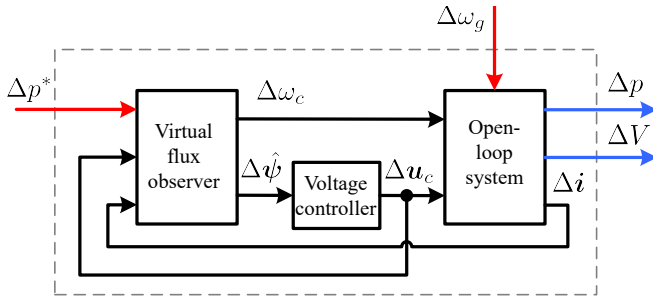


Fig. 4. Small-signal model of the closed-loop system.

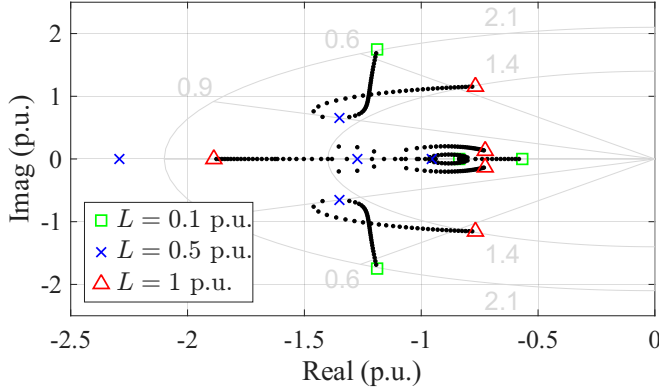


Fig. 5. Closed-loop pole trajectories of the proposed method under total impedance variation from $L = 0.1$ p.u. to $L = 1$ p.u..

V. SIMULATION RESULTS

In simulations, stability robustness of the proposed method is demonstrated in both frequency domain and time domain. The rated parameters of GCC and the base values are given in Table I.

A. Parameter tuning

The control parameters of the proposed method are designed as follows:

- 1) The closed-loop poles of flux estimation σ_o are assigned by k_o around $s = -2.5\omega_0$, through Eq. (17).
- 2) In Eq. (24), k_p is given by $\zeta = 0.9$ and $\omega_s = 1.5\omega_0$.
- 3) The closed-loop poles of voltage control σ_v are assigned by k_v around $s = -\omega_0$, through Eq. (30).

The operating point δ^* used in control parameter calculations is given by Eq. (8) where $p^* = 1$ p.u. and $L_0 = 0.5$ p.u.. The same control parameters are used throughout the simulation and experimental studies of this paper.

The varying grid strength is configured by varying total impedance L from 0.1 p.u. to 1 p.u., *i.e.*, short-circuit ratio (SCR) from 10 to 1.

B. Result and discussion

Fig. 5 shows the pole trajectories of the small-signal closed-loop system when $L_0 = 0.5$ p.u. is used in the proposed controller, while the actual impedance L varies from 0.1 to 1 p.u.. It can be observed that the poles experience small range

TABLE I
RATED PARAMETERS OF THE EXPERIMENTAL PLATFORM

Parameter	Actual value	Per unit value
Rated power	20 kVA	1 p.u.
Rated voltage	$\sqrt{2/3} \times 380$ V	1 p.u.
Rated current	$\sqrt{2} \times 30$ A	1 p.u.
Base inductance	23 mH	1 p.u.
Base frequency	50 Hz	1 p.u.
Filter impedance	2.5 mH	0.1 p.u.
Switching/Sampling frequency	10 kHz	200 p.u.
Rated DC-link voltage	750 V	2.4 p.u.

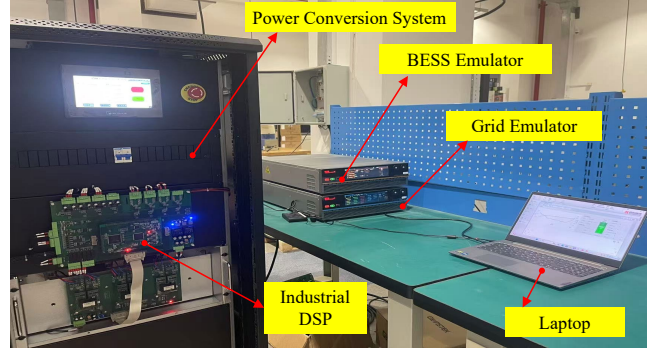


Fig. 6. Experimental platform with the 20 kVA PCS, grid emulator and BESS emulator.

excursions on the left half plane, thus maintaining stability. When the grid strength is very strong or very weak, the dynamic response of the proposed method will be slower than designed, as the dominant pole moves from $s = -\omega_0$ when $L = 0.5$ p.u. to $s = -0.6\omega_0$ when $L = 1$ p.u. and 0.1 p.u..

VI. EXPERIMENTAL RESULTS

A. Experimental setup

In the following, the proposed GFM controller is validated on a 20 kVA power conversion system (PCS) experimental platform, as shown in Fig. 6. The PCS mainly comprises a 3-phase 2-level power converter and a digital signal processor (DSP) TMS320F28335, on which the proposed GFM controller is implemented. The DC-side of the PCS is connected to a battery energy storage system (BESS) emulator. The AC-side is connected to a grid emulator. A variable impedance cabinet serves as variable grid impedance. The parameters of the experimental platform are given in Table I. The results are measured with an oscilloscope at sampling rate 25 kHz.

For comparison, the reference feedforward power synchronization control (RFPSC) method [10] is also implemented in the experiments. The control parameters are selected as $R_a = 0.2$ p.u. and $\omega_b = 0.1$ p.u. [5], [10].

B. Results and discussions

First, the control performance of the proposed method is compared with RFPSC when $L = L_0 = 0.5$ p.u. in Fig. 7. The active power set-point is first stepped up to 0.5 p.u., then to 1 p.u., and finally stepped down to 0. From Fig. 7(a), both methods track the power reference accurately. Their

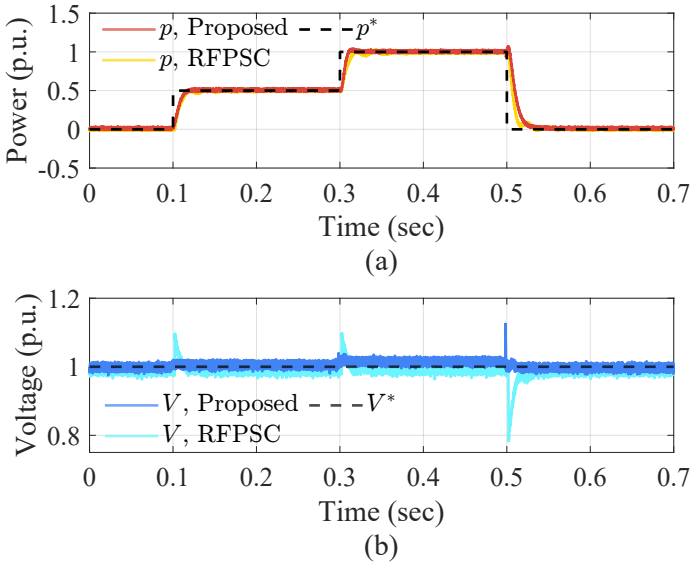


Fig. 7. Comparison of active power reference tracking performance between the proposed method and RFPSC when $L = 0.5$ p.u..

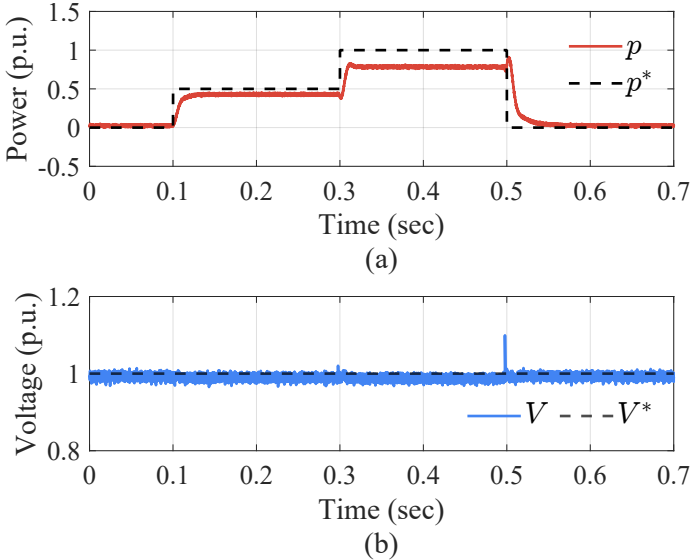


Fig. 8. Control performance of the proposed method when $L = 1$ p.u..

dynamic responses are also similar, with no overshoot and the settling time is around 0.02 s. However, the proposed method is more advantageous than RFPSC in PCC voltage response, as shown in Fig. 7(b). With the proposed method, there are no obvious voltage peaks during active power step-ups. In contrast, RFPSC produces 0.1 p.u. increases in PCC voltage at 0.1 s and 0.3 s, which only settle down after 0.02 s along with the transients of active power. Similarly, during active power step-down, PCC voltage drops lower than 0.8 p.u. with RFPSC, and takes 0.05 s to recover. With the proposed method, it is increased to 1.1 p.u. and restored within 0.01 s.

Next, stability robustness of the proposed method to grid strength variation is validated. Fig. 8 shows the control performance of the proposed method under weak grid condition

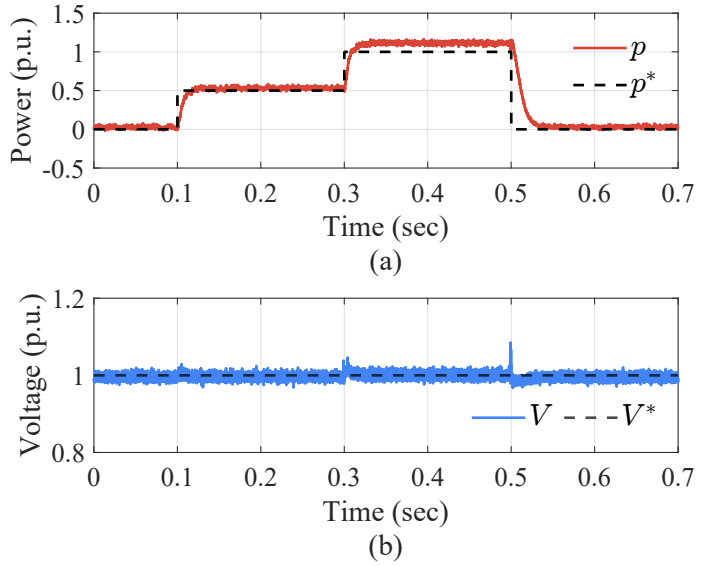


Fig. 9. Control performance of the proposed method when $L = 0.1$ p.u..

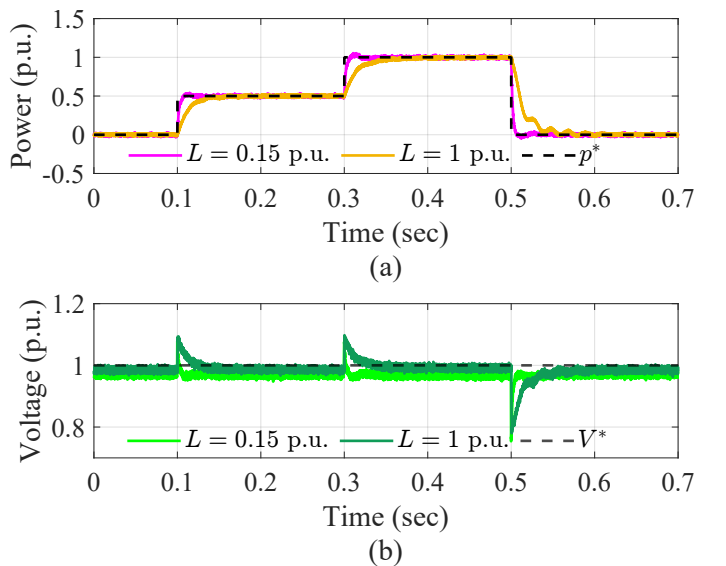


Fig. 10. Control performance of RFPSC when $L = 0.15$ p.u. and 1 p.u..

$L = 1$ p.u.. In Fig. 8(a), active power offsets occur due to plant parameter mismatch, which is common for observer-based controller and can be eliminated by identification of actual parameters or disturbance compensation algorithms. Meanwhile, the dynamic performance is robust to total impedance variation, by comparing the active power transients in Fig. 8(a) and Fig. 7(a). As L changes from design parameter 0.5 p.u. to 1 p.u., the active power response remains damped with slightly increased settling time. In Fig. 8(b), the advantage of stiff PCC voltage magnitude of the proposed method is also preserved under weak grid condition.

Similar conclusions can be drawn from Fig. 9, where total impedance changes to $L = 0.1$ p.u. to form weak grid condition. Despite the 0.1 p.u. offset in active power, the

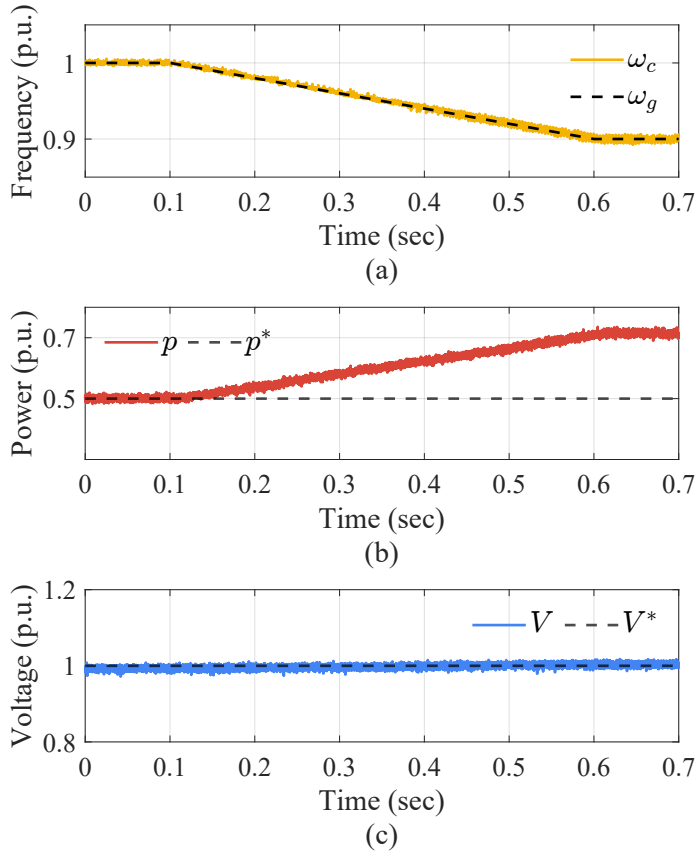


Fig. 11. Synchronization and control performance of the proposed method when grid frequency is ramped from 50 Hz to 45 Hz, $L = 0.5$ p.u..

transient response in Fig. 9(a) is almost identical with the accurate impedance case in Fig. 7(a). In Fig. 9(b), PCC voltage magnitude exhibits short transients of 0.01 s during step-up and step-down of 1 p.u. active power, which is slightly increased compared to medium and weak grid strengths.

To better demonstrate the robustness of the proposed method, the control performances of RFPSC under weak and strong grid conditions are compared in Fig. 10 for reference. The deviation of dynamic response of the two cases is evident. The settling time of active power and PCC voltage is increased from 0.01 s in strong grid condition, to 0.05 s in weak grid condition. In contrast, with the proposed method, the settling time of active power remains around 0.02 s across the range, and the stiff voltage source characteristic of PCC voltage is maintained in weak and strong grid alike.

Finally, synchronization and output response of the proposed method during grid frequency variation is demonstrated in Fig. 11. Fig. 11(a) shows that the rotating frequency of controller coordinate frame ω_c closely follows the decreasing grid frequency ω_g with no visible transient. In response to the frequency drop, active power output of GCC is ramped up from its set-point of 0.5 p.u. to 0.7 p.u. smoothly, as shown in Fig. 11(b), while the PCC voltage is only slightly increased from the set-point in Fig. 11(c). Notably, the active power offset induced by frequency mismatch corresponds to a droop

coefficient of $D_p = 2$ p.u. in the proposed GFM controller.

In conclusion, the experimental results demonstrate the robust dynamic performance of the proposed method across a wide range of grid strengths. With the proposed GFM controller, the GCC exhibits stiff voltage source behavior and droop characteristics.

REFERENCES

- [1] D. B. Rathnayake, M. Akrami, C. Phurailatpam, S. P. Me, S. Hadavi, G. Jayasinghe, S. Zabihi, and B. Bahrani, "Grid forming inverter modeling, control, and applications," *IEEE Access*, vol. 9, pp. 114781–114807, 2021.
- [2] R. Rosso, X. Wang, M. Liserre, X. Lu, and S. Engelken, "Grid-forming converters: Control approaches, grid-synchronization, and future trends—a review," *IEEE Open J. Ind. Appl.*, vol. 2, pp. 93–109, 2021.
- [3] R. H. Lasseter, Z. Chen, and D. Pattabiraman, "Grid-forming inverters: A critical asset for the power grid," *IEEE J. Emerg. Sel. Topics Power Electron.*, vol. 8, no. 2, pp. 925–935, 2020.
- [4] L. Zhang, L. Harnefors, and H.-P. Nee, "Power-synchronization control of grid-connected voltage-source converters," *IEEE Trans. Power Syst.*, vol. 25, no. 2, pp. 809–820, 2010.
- [5] L. Harnefors, M. Hinkkanen, U. Riaz, F. M. M. Rahman, and L. Zhang, "Robust analytic design of power-synchronization control," *IEEE Trans. Ind. Electron.*, vol. 66, no. 8, pp. 5810–5819, 2019.
- [6] X. Wang, M. G. Taul, H. Wu, Y. Liao, F. Blaabjerg, and L. Harnefors, "Grid-synchronization stability of converter-based resources—an overview," *IEEE Open J. Ind. Appl.*, vol. 1, pp. 115–134, 2020.
- [7] Y. Li, Y. Gu, and T. C. Green, "Revisiting grid-forming and grid-following inverters: A duality theory," *IEEE Trans. Power Syst.*, vol. 37, no. 6, pp. 4541–4554, 2022.
- [8] F. Zhao, T. Zhu, Z. Li, and X. Wang, "Low-frequency resonances in grid-forming converters: Causes and damping control," *IEEE Trans. Power Electron.*, vol. 39, no. 11, pp. 14430–14447, 2024.
- [9] X. Gao, D. Zhou, A. Anvari-Moghaddam, and F. Blaabjerg, "Stability analysis of grid-following and grid-forming converters based on state-space modelling," *IEEE Trans. Ind. Appl.*, vol. 60, no. 3, pp. 4910–4920, 2024.
- [10] L. Harnefors, F. M. M. Rahman, M. Hinkkanen, and M. Routimo, "Reference-feedforward power-synchronization control," *IEEE Trans. Power Electron.*, vol. 35, no. 9, pp. 8878–8881, 2020.
- [11] F. Zhao, T. Zhu, L. Harnefors, B. Fan, H. Wu, Z. Zhou, Y. Sun, and X. Wang, "Closed-form solutions for grid-forming converters: A design-oriented study," *IEEE Open J. Power Electron.*, vol. 5, pp. 186–200, 2024.
- [12] L. Harnefors, J. Kukkola, M. Routimo, M. Hinkkanen, and X. Wang, "A universal controller for grid-connected voltage-source converters," *IEEE Trans. Emerg. Sel. Topics Power Electron.*, vol. 9, no. 5, pp. 5761–5770, 2021.
- [13] T. Liu and X. Wang, "Unified voltage control for grid-forming inverters," *IEEE Trans. Ind. Electron.*, vol. 71, no. 3, pp. 2578–2589, 2024.
- [14] T. Nurminen, R. Mourouvin, M. Hinkkanen, J. Kukkola, M. Routimo, A. Vilhunen, and L. Harnefors, "Observer-based power-synchronization control for grid-forming converters," in *2023 IEEE Belgrade PowerTech*, pp. 1–6, 2023.
- [15] T. Nurminen, R. Mourouvin, M. Hinkkanen, and J. Kukkola, "Multifunctional grid-forming converter control based on a disturbance observer," *IEEE Trans. Power Electron.*, vol. 39, no. 10, pp. 13023–13032, 2024.
- [16] T. Nurminen, R. Mourouvin, M. Hinkkanen, and J. Kukkola, "Design and sensitivity analysis of grid-forming converter control based on a disturbance observer," *IEEE Trans. Ind. Appl.*, pp. 1–13, 2025.
- [17] M. Hinkkanen, S. E. Saarakkala, H. A. A. Awan, E. Mölsä, and T. Tuovinen, "Observers for sensorless synchronous motor drives: Framework for design and analysis," *IEEE Trans. Ind. Appl.*, vol. 54, no. 6, pp. 6090–6100, 2018.
- [18] M. Zhang, B. Xia, and J. Zhang, "Parameter design and convergence analysis of flux observer for sensorless PMSM drives," *IEEE Trans. Energy Convers.*, vol. 37, no. 4, pp. 2512–2524, 2022.